Supplementary document to the manuscript titled: Chordwise flexible aft-tail suppresses jet-switching by reinstating wake periodicity in a flapping foil

1. Various measures to establish the wake dynamics

1.1. *Measures to characterise jet-switching*

The vortex street behind the heaving foil is characterized as upward or downward deflected, based on the overall wake deflection angle, Θ (Godoy-Diana *et al.* 2009; Majumdar *et al.* 2020). As schematically shown in Fig. 1(a), the angle between the mean position of the heaving motion (denoted by the dashed-dotted line) and the average deflection direction of the wake (denoted by the dashed line) gives the deflection angle (Θ) of the vortex street. Upward and downward deflected wakes are indicated by the positive and negative values of Θ, respectively. To understand the mechanism of jet-switching, a system of the first three vortices present in the wake at the end of a flapping cycle is considered; see Fig. 1(b). Here, vortices **A**, **B**, and **C** refer to the first counter-clockwise (CCW), first clockwise (CW) and the second CCW vortex, respectively. As the flow evolves, if the distance between vortices **A** and **B** becomes less than that of **B** and **C**, then vortex couple **A-B** forms the dominant upward deflecting couple. It eventually deflects the entire wake in the upward direction in the subsequent cycles, which is the direction of its self-induced dipole velocity (Majumdar *et al.* 2020). The opposite scenario takes place during the formation of **B-C**, the dominant downward deflecting couple, which induces the wake to deflect downward. They will be referred to as 'symmetry breaking couples' here. The mutual competition between these two symmetry-breaking couples eventually dictates the overall deflection direction of the wake (Godoy-Diana *et al.* 2009; Zheng & Wei 2012). The dominance of either **A-B** or **B-C** is illustrated using the ratio of their self induced dipole velocities. It is defined as U_{dipole}-ratio $= U_{\text{dipole,AB}}/U_{\text{dipole,BC}}$, where U_{dipole} is the self induced dipole velocity and evaluated as (Saffman 1995; Anderson Jr 2010)

$$U_{\text{dipole}} = \frac{\Gamma_{\text{avg}}}{2\pi\xi}. \tag{1.1}$$

Here, ξ denotes the distance between the two partners of a vortex couple, and Γ_{avg} is the average of the absolute circulation values of the two partners. U_{dipole}-ratio can be evaluated as the ratio of two quantities, Γ_{avg}-ratio (defined as $\Gamma_{\text{avg,AB}}/\Gamma_{\text{avg,BC}}$) and ξ-ratio (defined as $\xi_{\text{AB}}/\xi_{\text{BC}}$). Throughout this paper, terms 'AB' or 'BC' added in the suffix of any quantity/measure designates that particular quantity/measure to be associated with couples **A-B** or **B-C**, respectively. The following section discusses the procedure of locating center in regular and irregular types of vortices and calculation of ξ in detailed.

1.2. *Computation procedure for ξ and Γ*

For any two wake vortices, say **A** and **B**, the distance between them is calculated as,

$$\xi_{\text{AB}} = \sqrt{(x_{\text{A}} - x_{\text{B}})^2 + (y_{\text{A}} - y_{\text{B}})^2}, \tag{1.2}$$

where, $(x_{\text{A}},\ y_{\text{A}})$ and $(x_{\text{B}},\ y_{\text{B}})$ are the coordinates of the centres of vortices **A** and **B**, respectively. For any particular vortex under investigation, a rectangular region of arbitrary size (shown using black dashed lines in Figs. 2(a), and 3 of this document) is considered such that it includes the vortex entirely but does not contain portion of any other individual vortex. Next, the vortex centres are identified by carrying out a search of local maxima (for anti-clockwise vortex) and minima (for clockwise vortex) in the vorticity field. When there

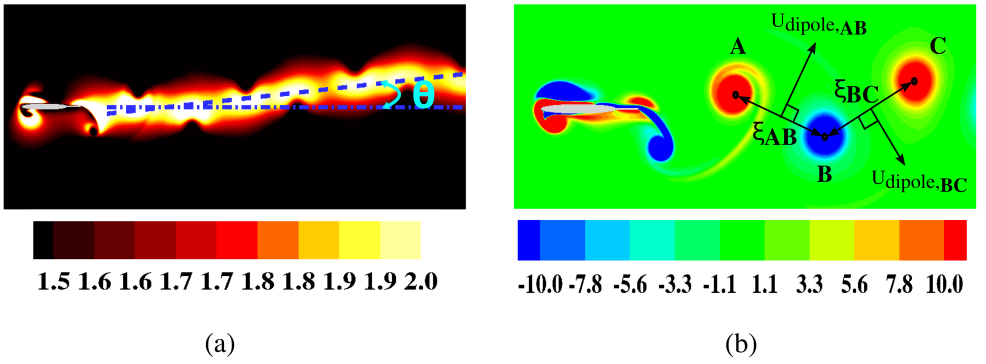

Figure 1: (a) Definition of the deflection angle (Θ), (b) schematic representation of the system of first three vortices in the trailing-wake used in the present analysis

.

exist multiple local extremum within the chosen region, then the location corresponding to the higher magnitude is taken as the centre location. This kind of situation may emerge in the flow-field where the vorticity distribution is irregular due to the merging of a small vortex with a larger vortex of the same sense of rotation as shown in Fig. 2(a). In this case, the location corresponding to the minima with higher magnitude is taken as the centre of the merged vortex system.

Once the vortex centres are found, the circulation (Γ) is calculated by performing a vorticity area integration over a rectangular region (shown using red and blue solid lines in Figs. 2(a) and 3, respectively) around the vortex. The length and width of this rectangular zone is determined by using Gaussian fits, $(1/(\sigma_i\sqrt{2\pi}))\exp(-(x_i-\mu)^2/(2{\sigma_i}^2))$, of the vorticity-field data along the horizontal and vertical axes, respectively, centered at the vortex centre. Figs. 2(b) and 2(c) show the vorticity data and the corresponding Gaussian fit towards the right and top sides of the rectangular zone for a typical vortex example shown in Fig. 2(a). For the other two sides (left and bottom) the same pattern is followed. The distance of each side of the rectangular region is selected in such a way that the vortex strength at the boundary becomes 2% of the vortex strength at the center. The typical reconstructed rectangular boundary for the irregular and regular vortices are shown in Fig. 2(a) and Fig. 3 (red and blue solid lines), respectively. The same procedure is followed in determining ξ and Γ for every vortex structure. For more discussion on the above mentioned quantities, please refer to Godoy-Diana *et al.* (2009); Zheng & Wei (2012); Wei & Zheng (2014); Majumdar *et al.* (2020).

2. Measures to characterise the dynamical states through time series analysis

Different dynamical states (such as periodicity, quasi-periodicity, intermittency, etc.) of the flow-field at different parametric regimes are identified here through time series analysis of the aerodynamic loads. Please note that the classical topological measures from the dynamical systems theory, such as Lyapunov exponents or correlation dimensions require significantly long time history data to obtain converged values. Generating such a long time-history data through high fidelity N-S solvers may involve prohibitively large computational time and cost. In contrast, time series tools such as reconstructed phase portrait (Kennel *et al.* 1992), frequency spectra, Morlet wavelet transform (Grossmann *et al.* 1990) and Recurrence Plots (Marwan *et al.* 2007) can conclusively establish the dynamical state even from relatively shorter time histories. Also, for certain dynamical states, time series measures could be more

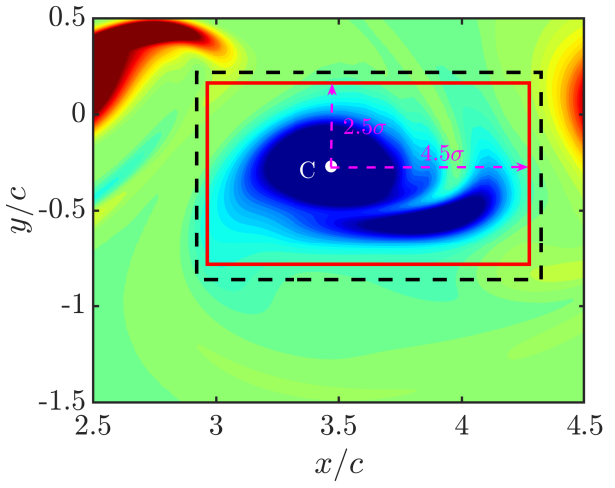

(a) Rectangular zones covering an irregular vortex for finding the location of the center (black dashed line), and circulation computation (red solid lines).

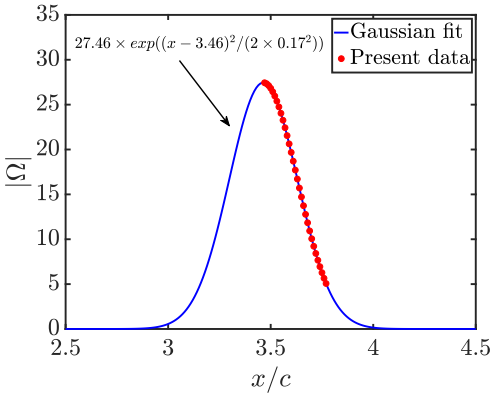

(b) Gaussian fit towards the right side of the center.

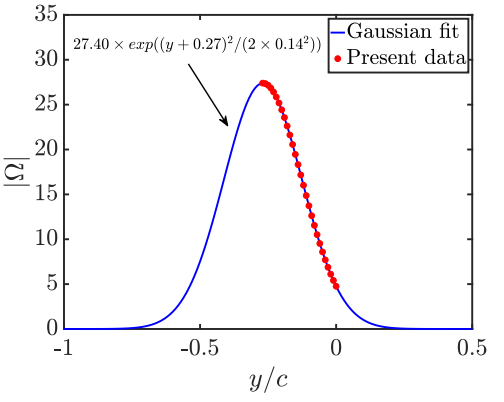

(c) Gaussian fit towards the top side of the center.

Figure 2: Process to determine the centre of vortex.

conclusive than classical chaos tools. Due to these various advantages, the latter measures are used in the present study. Dynamics are discussed using the C_D time-series data, even though the same dynamical features are reflected in both C_L and C_D. This is done for the sake of brevity and also because the dynamical signatures seem more prominent in C_D.

2.1. *Phase space reconstruction and Morlet wavelet transform*

To derive the phase space and characterise the system attractors, time histories of loads are used for phase-space reconstruction using the time-delay embedding theorem proposed by Takens (1981). A reconstruction matrix ($\mathbf{Z}$) for C_D is evaluated as,

$$\mathbf{Z} = \begin{bmatrix} C_D(t) & C_D(t+\tau_{\text{opt}}) & C_D(t+2\tau_{\text{opt}}) & C_D(t+3\tau_{\text{opt}}) & \dots & C_D(t+(d_m-1)\tau_{\text{opt}}) \end{bmatrix}. \tag{2.1}$$

were, τ_{opt} indicates the optimum time delay and d_m denotes minimum embedding dimension. The τ_{opt} is the time delay which produces independent coordinates in the reconstructed phase-space, and is selected based on the first local minima in the average mutual information (AMI)

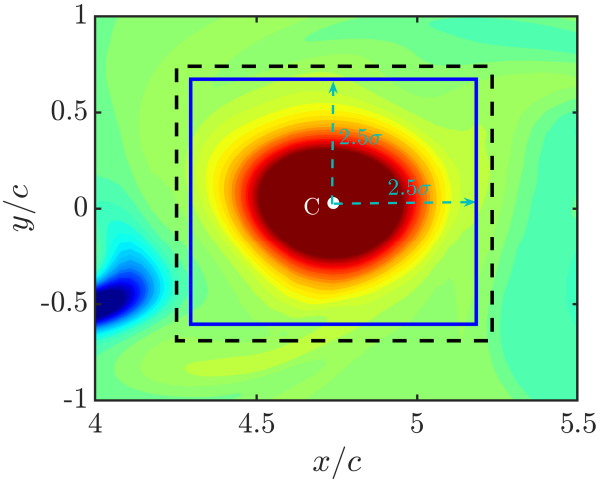

Figure 3: Rectangular zones covering a regular vortex for finding the location of the center (black dashed line) and circulation computation (blue solid lines).

vs. time delay (τ) plot (Fraser & Swinney 1986). For a given τ, AMI indicates the extent to which $C_D(t+\tau)$ is related to $C_D(t)$, and can be calculated using the following equation,

$$\mathrm{AMI}(\tau) = \sum_{i,j} P\left(C_{D_i}(t),\, C_{D_j}(t+\tau)\right) \log_2 \left[\frac{P\left(C_{D_i}(t),\, C_{D_j}(t+\tau)\right)}{P\left(C_{D_i}(t)\right)\, P\left(C_{D_j}(t+\tau)\right)} \right], \tag{2.2}$$

where, $P(*)$ and $P(*,*)$ denote the marginal and joint probabilities of occurrence of $C_{D_i}(t)$ and $C_{D_j}(t+\tau)$ in the time series of the scalar variable. The AMI plot for a typical C_D data at $h = 0.375$ ($\kappa h = 1.5$) and $\gamma = 0.1$ is presented in Fig. 4(a). The optimum time delay is found to be $\tau_{\mathrm{opt}} = 0.24$. Notably the value of τ_{opt} is related to the dynamical characteristics of the time series data and could be different for different signals, e.g, the different C_D time histories corresponding to different parametric conditions presented in this study. This is demonstrated in Figs. 5 and 6. For the reconstruction of each time history, individual τ_{opt} value corresponding to that particular signal is evaluated first, and then the time data is reconstructed.

In Eq.(2.1), d_m refers to the minimum embedding dimension for which the percentage of false nearest neighbours (FNN) goes to zero (Kennel *et al.* 1992). The % of FNN can be evaluated as,

$$\%\ \text{of FNN} = \frac{\text{numbers of FNN in } d\text{−dimension space}}{\text{numbers of FNN in } 1\text{−dimension space}} \times 100\ \% \tag{2.3}$$

The discussion on identifying the false nearest neighbours is out of the scope of present study, and the readers are requested to refer to the original work of Kennel *et al.* (1992). The % of FNN plot, obtained from the same C_D data as used in AMI calculation, shows the minimum embedding dimension to be $d_m = 5$; see Fig. 4(b). Although the C_D time histories are reconstructed using $d_m = 5$, it is projected on a three-dimensional space for the sake of visual representation of the phase portraits. For further details regarding the computation of the above measures, please refer to the work of Juniper & Sujith (2018). A closed-loop orbit in the reconstructed phase-portrait is a signature of periodic dynamics; whereas, a

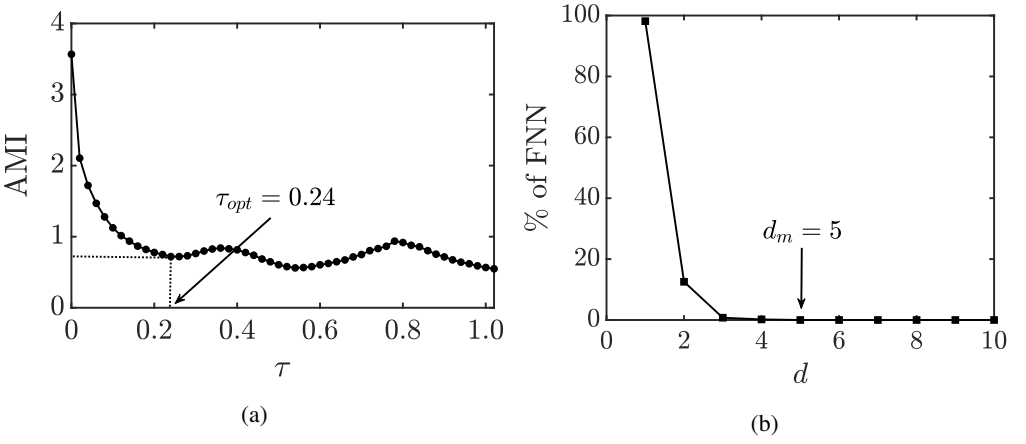

Figure 4: Time-delay embedding for reconstructing the phase-space trajectories: (a) optimum time delay, (b) minimum embedding dimension.

toroidal attractor indicates quasi-periodicity. However, reconstructed phase portraits may not be adequate to capture the dynamical state of intermittency. For that, the recurrence plots are more useful as described in the following subsection.

The Morlet wavelet transform (Grossmann *et al.* 1990) shows the time-frequency behaviour of a signal on a scalogram plot where the x and y-axes indicate the time and frequency content of the signal, respectively. In the scalogram plot, a narrow frequency indicates periodicity; whereas, the presence of incommensurate frequency bands designates quasi-periodic dynamics and a broad-banded frequency spectra is the signature of chaos.

2.2. *Recurrence Plots*

Recurrence plots (RPs) (Marwan *et al.* 2007) have been proven to be a robust and effective tool for qualitatively distinguish between different dynamical states, especially for establishing the dynamical state of intermittency (Badrinath *et al.* 2017; Bose *et al.* 2021). A binary recurrence matrix $R_{i,j}$ is calculated as,

$$R_{i,j} = \mathbf{H}\left(\epsilon - ||z_i - z_j||\right); \quad i, j = 1, 2, 3, ..., N_1, \tag{2.4}$$

where, z_i and z_j are the reconstructed phase-space vectors of d_m–dimension, $\mathbf{H}$ is the Heaviside step function, ϵ is a predefined threshold, and N_1 is the total number of phase-space points; $||\,.\,||$ indicates the Euclidean L_2-norm. In the current study, ϵ is considered as 10% of the reconstructed phase-space diameter, where the diameter refers to the distance between the two farthest points in the phase-space. RP contains black and white points corresponding to ones and zeros, respectively; $R_{i,j}$ in the recurrence matrix is considered to be zero if the distance between the two points z_i and z_j in the reconstructed phase-space is greater than ϵ, else it is considered to be unity. This binary matrix is graphically represented on a 2D plot called the RP. Note that RP corresponding to a periodic signal displays equidistant solid lines parallel to the main diagonal, whereas the quasi-periodicity is characterised by unequally spaced lines. Short and broken diagonal lines along with isolated scattered points are the signature of chaos. The intermittency behaviour is reflected through alternative windows of different dynamical states over the main diagonal in RP.

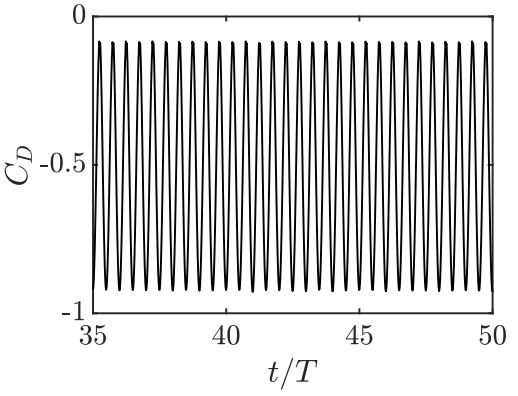

(a) Rigid aft-tail at κh = 1.0 (κ = 4.0)

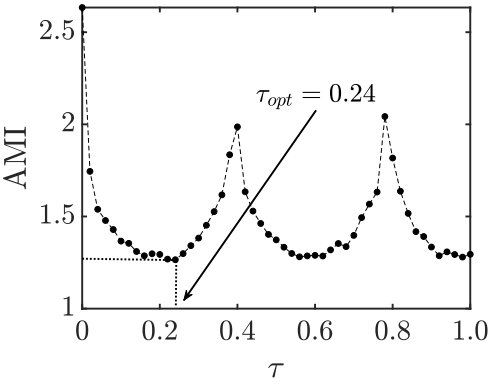

(b) Optimum time delay for the signal in (a)

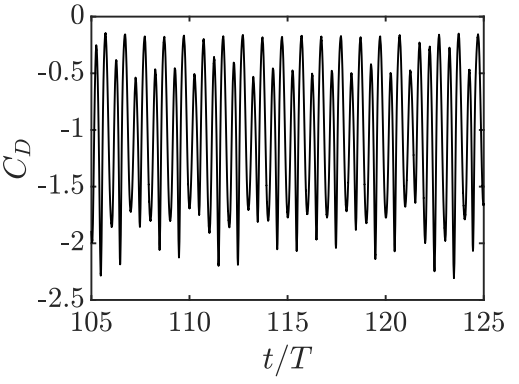

(c) Rigid aft-tail at κh = 1.2 (κ = 4.0)

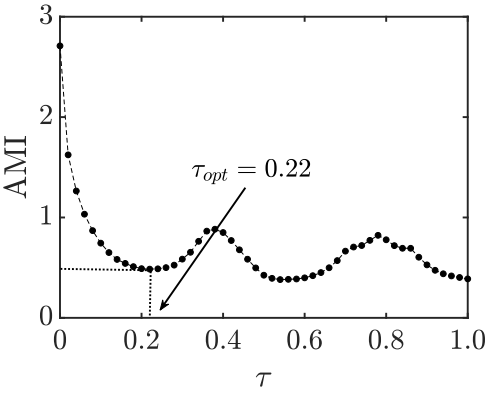

(d) Optimum time delay for the signal in (c)

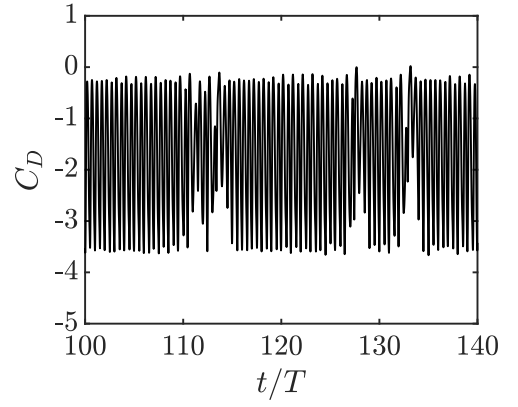

(e) Rigid aft-tail at κh = 1.5 (κ = 4.0)

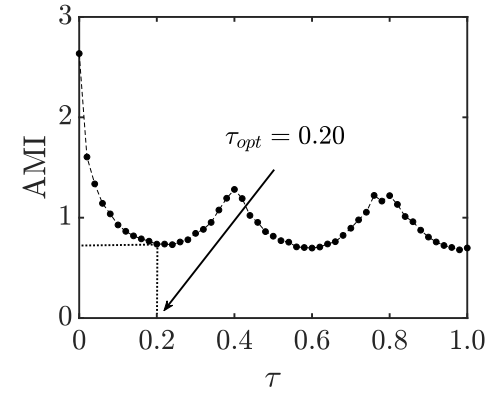

(f) Optimum time delay for the signal in (e)

Figure 5: (a, c, e) C_D time histories at different κh for the rigid tail configuration; (b, d, f) respective AMI vs time-delay plots.

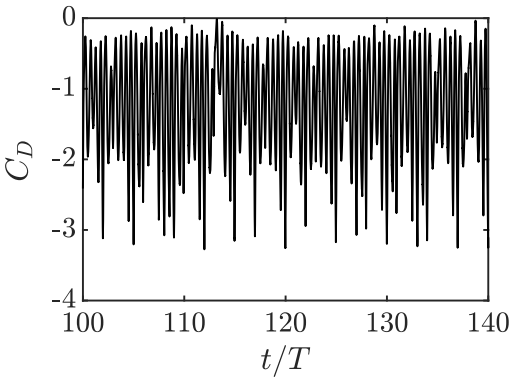

(a) Flexibility level I aft-tail at $\kappa h = 1.5$ ($\kappa = 4.0$)

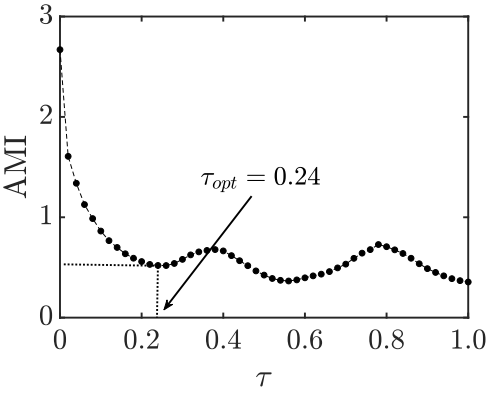

(b) Optimum time delay for the signal in (a)

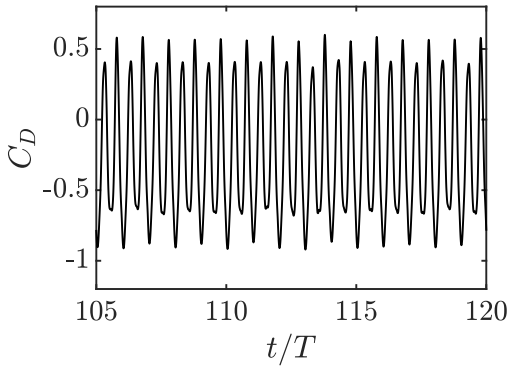

(c) Flexibility level II aft-tail at $\kappa h = 1.5$ ($\kappa = 4.0$)

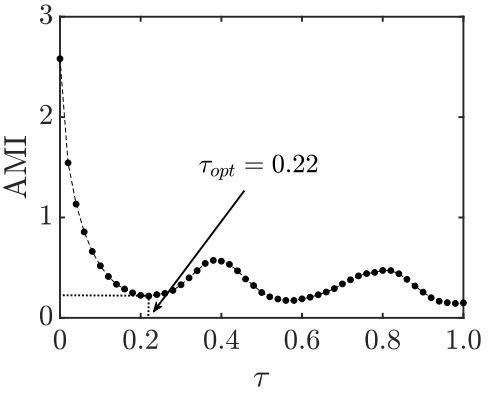

(d) Optimum time delay for the signal in (c)

Figure 6: (a, c) C_D time histories at $\kappa h = 1.5$ for different flexible tail configurations; (b, d) respective AMI vs time-delay plots.

2.3. *Recurrence quantification analysis*

The quantitative measures are developed from RPs based on the recurrence point density and the structure of recurrence patterns for Recurrence quantification analysis (RQA) (Marwan *et al.* 2007). RQA has been used, in terms of several other measures of complexity, to quantify the small-scale structures in the RP. In the present study, we have used three different measures: determinism (DET), recurrence rate (RR) and laminarity (LAM). These measures are based on the recurrence point density and the diagonal line structures of the RP; refer to Marwan *et al.* (2007) for more details. Table 1 presents the RQA measures for different aft-tail configurations considered in this study.

The percentage of recurrence points forming the diagonal lines is called DET, and is used as determinism or predictability measure of the system. The formulation of DET is given as;

$$DET = \frac{\sum_{l=l_{min}}^{N_l} lP(l)}{\sum_{l=1}^{N_l} lP(l)}, \tag{2.5}$$

where l_{min} is the threshold set to 2 points in the RP, which excludes the diagonal lines formed by the tangential motion of a phase space trajectory (Schultz *et al.* 2015), and $P(l)$ is the histogram of the lengths l of the diagonal lines. The maximum value of DET is 100%

Table 1: Recurrence Quantification Analysis (RQA) measures

	DET (%)	RR	LAM (%)
Rigid aft-tail	91.8438	2.0994×10^{-4}	9.3621
Flexibility level I	95.4852	3.0593×10^{-3}	38.0310
Flexibility level II	98.9469	0.012	69.7128

which corresponds to a periodic state with all the recurrent points are along the diagonals; whereas, chaotic signals have a low value of DET since they are characterized by short diagonal structures in RP. Table 1 shows that the DET value is relatively lower for the rigid tail configuration, indicating the corresponding aperiodic state of the wake. On the other hand, periodicity of the wake in case of the flexibility level II aft-tail is confirmed by the DET value being very close to 100%. DET is a complementary measure to the time spent by the system trajectories in the chaotic regime. The higher values of DET are indicative of the fact that the system trajectories spend lesser time in the chaotic regime.

The definition of RR is given by

$$RR = \frac{1}{{N_1}^2} \sum_{i,j=1}^{N_1} R_{i,j}. \tag{2.6}$$

RR is is a measure of the density of recurrence points in a recurrence plot, where N_1 is the number of points in the phasespace. As $N_1 \to \infty$, RR gives the probability that the state returns to its ϵ–neighbourhood (ϵ is the threshold used while computing RP). Therefore, RR is expected to be lower for chaotic signal than that of the periodic signal. A considerable decrease in the RR value is observed for the rigid aft-tail as compared to the flexibility level II aft-tail, which marks the transition in the system from aperiodic to periodic states.

LAM is defined as the percentage of recurrence points forming the vertical lines and is given as,

$$LAM = \frac{\sum_{v=v_{min}}^{N_1} vP(v)}{\sum_{v=1}^{N_1} vP(v)}, \tag{2.7}$$

where $P(v)$ is the histogram of the lengths v of the vertical lines and v_{min} is the threshold set to 2 points in the RP. Similar to DET, larger values of LAM correspond to the periodic signals and lower values correspond to chaotic signals. The LAM for the rigid tail configuration is found to be significantly lower as compared to the flexibility level II in this study; see Table 1. This is representative of the dynamical transition taking place in the system due to the presence of tail-flexibility. Therefore, the RQA measures provide a good indication of dynamical transitions and can be used as precursors in this regard.

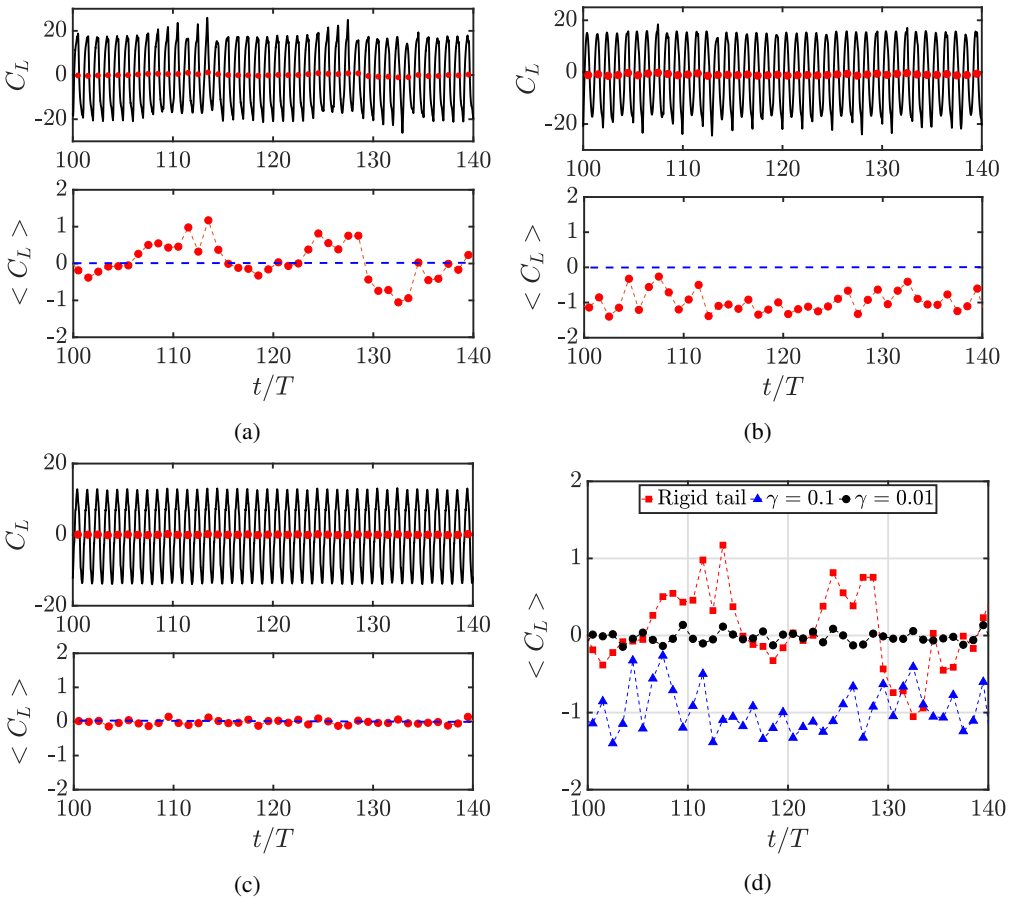

Figure 7: Time variation in the lift coefficient (C_L) and the period-averaged lift coefficient ($< C_L >$) for (a) rigid tail, (b) flexibility level I, (c) flexibility level II; and (d) shows direct comparison of $< C_L >$ for different aft-tail configurations.

3. Period averaged force characteristics and propulsive performance

The period-averaged lift coefficient ($< C_L >$) along with the corresponding C_L time histories are plotted in Fig. 7 of this response document for the three different aft-tail configurations. The trailing-wake jet-switching in the case of rigid-tail directly reflects on the lift force behaviour as $< C_L >$ changes its sign ; see Fig. 7(a). As flexibility is introduced (level I) in the aft-tail, $< C_L >$ always maintains the same sign even though the magnitude varies with time (Fig. 7(b)). In the case of flexibility level II, as the jet-switching and wake deflection get inhibited, the $< C_L >$ settles approximately near zero (Fig. 7(c)), and its significant variation as was seen in earlier two cases, gets substantially reduced. These results for C_L are consistent with the behaviour of the wake (deflected to almost symmetric).

The period-averaged drag coefficient ($< C_D >$) is plotted and compared for the three different aft-tails in Fig. 8. The rigid tail set-up maintains higher thrust values in most of the flapping cycles except during the intermittent chaotic bursts; see Fig. 8a. In this case, $< C_D >$ takes values approximately near to $< C_D >= -1.75$ during the quasi-periodic windows, whereas in the chaotic windows $< C_D >$ displays unpredictable fluctuation. The negative sign is indicative of the net positive thrust. At flexibility level I, thrust is seen to decrease a little compared to the rigid tail case. Finally, $< C_D >$ becomes almost constant

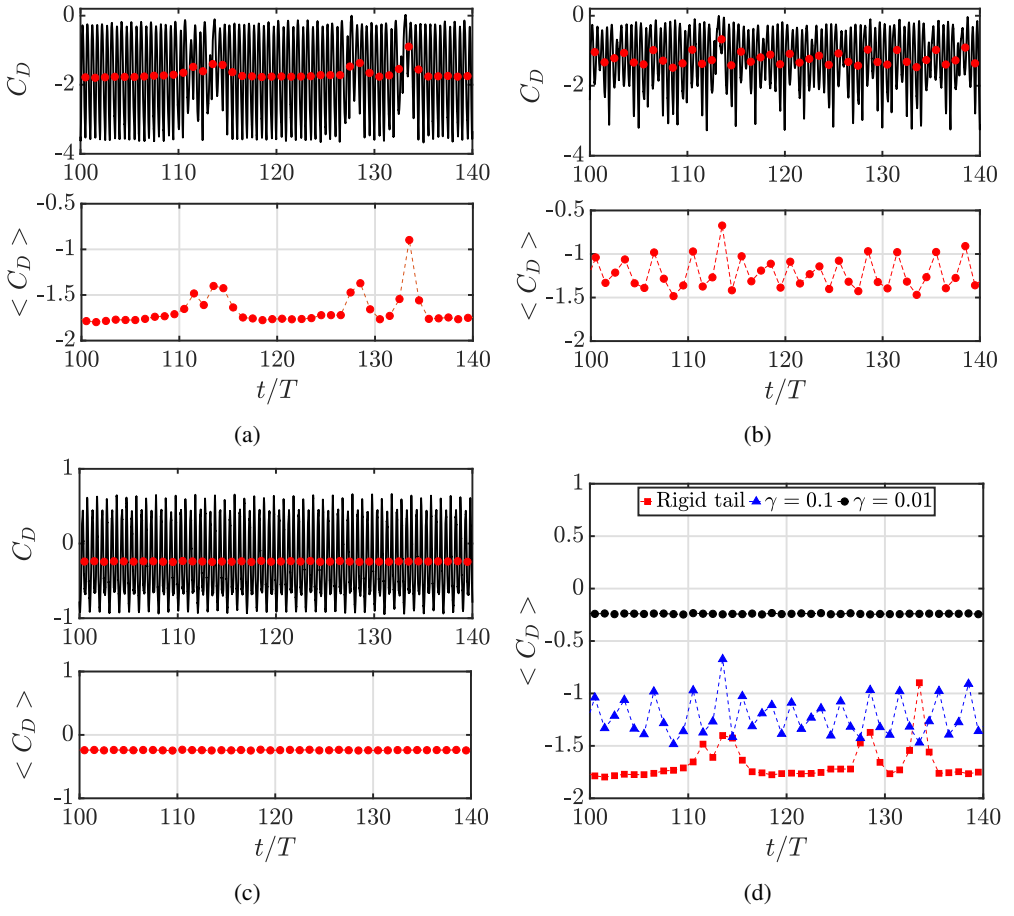

Figure 8: Time variation in the drag coefficient (C_D) and the period-averaged drag coefficient ($< C_D >$) for (a) rigid tail, (b) flexibility level I, (c) flexibility level II, and (d) comparison of $< C_D >$ for different aft-tail configurations.

in the case of flexibility level II during the entire time range and indicates a reduction in the thrust. The corresponding propulsive efficiencies are computed using the formulation given by Lewin & Haj-Hariri (2003) and values are presented in Table 2. Note that the flexibilities chosen were instrumental in regularising the aperiodicity in the flow-field and are not exactly of the same orders as mostly presented in the existing literature.The thrust behaviour needs further investigations to better comment on the optimal operating range.

4. Details of the supplementary videos

Continuous temporal evolution of the wake under different parametric conditions have been presented in the following videos.

4.1. *Supplementary 'Movie 1'*

This video presents the flow-field around a heaving foil with rigid aft-tail configuration at $\kappa h = 1.5$. In this video, wake is seen to change its deflection direction from downward to upward and vice-versa. This phenomenon of changing deflection direction of the vortex street is called jet-switching.

Table 2: Comparison of propulsive efficiency for different aft-tail configuration

Aft-tail configuration	Input work (W_i)	Output work (W_o)	Propulsive efficiency ($\eta = -W_o/W_i \times 100\%$)
Rigid tail	−12.044	1.715	14.239
Flexibility level I	−10.966	1.255	11.444
Flexibility level II	−8.804	0.247	2.805

4.2. *Supplementary 'Movie 2'*

This video presents the flow-field with an aft-tail of flexibility level I configuration at $\kappa h = 1.5$. In this video, wake is always seen to be deflected in the downward direction with varying angles of deflection. However, the wake deflection never turn upwards, thus it can be said that jet-switching is suppressed.

4.3. *Supplementary 'Movie 3'*

This video presents the flow-field with an aft-tail of flexibility level II configuration at $\kappa h = 1.5$. In this video, the trailing-wake shows a reverse Kàrmàn street without any switching or any significant deflection.

4.4. *Supplementary 'Movie 4'*

This video presents the flow-field with an aft-tail length $L_t = 0.38c$ of flexibility level I configuration at $\kappa h = 1.5$. In this video, the trailing-wake shows a reverse Kàrmàn street without any jet-switching and wake is mildly deflected upwards.

4.5. *Supplementary 'Movie 5'*

This video presents the flow-field around a heaving teardrop shaped foil in quiescent flow condition as per Heathcote & Gursul (2007); $h = 0.194$, $b/c = 1.13 \times 10^{-3}$, $Re_f = 300$. Note, symbols follow the same definitions as given in Heathcote & Gursul (2007), (equivalent $\gamma = 0.496$). In this video, the wake is seen to change its deflection direction signifying jet-switching as was also reported in the experiments of Heathcote & Gursul (2007).

REFERENCES

Anderson Jr, John David 2010 *Fundamentals of aerodynamics*. Tata McGraw-Hill Education.

Badrinath, S, Bose, C & Sarkar, S 2017 Identifying the route to chaos in the flow past a flapping airfoil. *European Journal of Mechanics-B/Fluids* **66**, 38–59.

Bose, C, Gupta, S & Sarkar, S 2021 Dynamic interlinking between near-and far-field wakes behind a pitching–heaving airfoil. *Journal of Fluid Mechanics* **911**, A31–1–36.

Fraser, AM & Swinney, HL 1986 Independent coordinates for strange attractors from mutual information. *Physical Review A* **33** (2), 1134.

Godoy-Diana, Ramiro, Marais, Catherine, Aider, Jean-Luc & Wesfreid, José Eduardo 2009 A

model for the symmetry breaking of the reverse bénard–von kármán vortex street produced by a flapping foil. *Journal of Fluid Mechanics* **622**, 23–32.

Grossmann, A, Kronland-Martinet, R & Morlet, J 1990 Reading and understanding continuous wavelet transforms. In *Wavelets*, pp. 2–20. Springer.

Heathcote, S & Gursul, I 2007 Jet switching phenomenon for a periodically plunging airfoil. *Physics of Fluids* **19** (2), 027104.

Juniper, MP & Sujith, RI 2018 Sensitivity and nonlinearity of thermoacoustic oscillations. *Annual Review of Fluid Mechanics* **50**, 661–689.

Kennel, MB, Brown, R & Abarbanel, HDI 1992 Determining embedding dimension for phase-space reconstruction using a geometrical construction. *Physical Review A* **45** (6), 3403.

Lewin, Gregory C & Haj-Hariri, Hossein 2003 Modelling thrust generation of a two-dimensional heaving airfoil in a viscous flow. *Journal of Fluid Mechanics* **492**, 339–362.

Majumdar, D, Bose, C & Sarkar, S 2020 Effect of gusty inflow on the jet-switching characteristics of a plunging foil. *Physics of Fluids* **32** (11), 117105.

Marwan, N, Romano, MC, Thiel, M & Kurths, J 2007 Recurrence plots for the analysis of complex systems. *Physics Reports* **438** (5-6), 237–329.

Saffman, Philip G 1995 *Vortex dynamics*. Cambridge university press.

Schultz, David, Spiegel, Stephan, Marwan, Norbert & Albayrak, Sahin 2015 Approximation of diagonal line based measures in recurrence quantification analysis. *Physics Letters A* **379** (14-15), 997–1011.

Takens, F 1981 Detecting strange attractors in turbulence. In *Dynamical System and Turbulence, Warwick 1980*, pp. 366–381. Springer, Berlin, Heidelberg.

Wei, Z & Zheng, ZC 2014 Mechanisms of wake deflection angle change behind a heaving airfoil. *Journal of Fluids and Structures* **48**, 1–13.

Zheng, Zhongquan Charlie & Wei, Z 2012 Study of mechanisms and factors that influence the formation of vortical wake of a heaving airfoil. *Physics of Fluids* **24** (10), 103601.